Empowering Smart Buildings with Self-Sensing Concrete for Structural Health Monitoring

Zheng Gong*†, Lubing Han*†¶, Zhenlin An†, Lei Yang†, Siqi Ding‡, Yu Xiang§
*Co-primary Student Authors
†Department of Computing, The Hong Kong Polytechnic University
¶School of Computer Science and Technology, Xi'an Jiaotong University
‡ School of Civil and Environmental Engineering, Harbin Institute of Technology, Shenzhen
§ Department of Civil and Environmental Engineering, The Hong Kong Polytechnic University
{gz,han,an,young}@tagsys.org,dingsiqi@hit.edu.cn,cee.yu.xiang@polyu.edu.hk

ABSTRACT

Given the increasing number of building collapse tragedies nowadays (e.g., Florida condo collapse), people gradually recognize that long-term and persistent structural health monitoring (SHM) becomes indispensable for civilian buildings. However, current SHM techniques suffer from high cost and deployment difficulty caused by the wired connection. Traditional wireless sensor networks fail to serve in-concrete communication for SHM because of the complexity of battery replacement and the concrete Faraday cage. In this work, we collaborate with experts from civil engineering to create a type of promising self-sensing concrete by introducing a novel functional filler, called EcoCapsule– a battery-free and miniature piezoelectric backscatter node. We overcome the fundamental challenges in in-concrete energy harvesting and wireless communication to achieve SHM via EcoCapsules. We prototype EcoCapsules and mix them with other raw materials (such as cement, sand, water, etc) to cast the self-sensing concrete, into which EcoCapsules are implanted permanently. We tested EcoCapsules regarding real-world buildings comprehensively. Our results demonstrate single link throughputs of up to 13 kbps and power-up ranges of up to 6 m. Finally, we demonstrate a long-term pilot study on the structural health monitoring of a real-life footbridge.

CCS CONCEPTS

• **Hardware → Wireless integrated network sensors**.

KEYWORDS

Structural Health Monitoring, Backscatter Communication, Ultrasonics

ACM Reference Format:
Zheng Gong*†, Lubing Han*†¶, Zhenlin An†, Lei Yang†, Siqi Ding‡, Yu Xiang§. 2022. Empowering Smart Buildings with Self-Sensing Concrete for Structural Health Monitoring. In *ACM SIGCOMM 2022 Conference (SIGCOMM '22), August 22–26, 2022, Amsterdam, Netherlands.* ACM, New York, NY, USA, 16 pages. https://doi.org/10.1145/3544216.3544270

1 INTRODUCTION

On June 24, 2021, Champlain Towers South, a 12-story beachfront condominium in the Miami suburb of Surfside, Florida, United States, partially collapsed, eventually resulting in a tragedy of 98 deaths [16] that shocked the whole world. According to the investigation, the main contributing factor to the collapse is the long-term reinforced concrete structural support degradation in the ground-level parking garage under the housing units. This degradation is due to water penetration and corrosion of the reinforcing steel. Nowadays, safe and dependable architectures play fundamental and crucial roles in modern society, particularly for the historical buildings established hundreds of years ago. However, concrete architectures inevitably suffer from aging and environmental degradation. The best approach to preventing buildings from abrupt collapse is to conduct structural health monitoring (SHM), an in-service health assessment for a structure through an automated sensing system.

SHM provides a practical tool for ensuring integrity and safety, detecting the evolution of damage, and estimating performance deterioration of civil infrastructures. The concept of SHM is not new. Tracing a building's structure in real-time has been a long-standing vision. Thus, further structural deviation and damage are quickly prevented if risks are detected. In the field of civil engineering, four sensing solutions are currently employed for SHM [56], as shown in Fig. 1. In particular, (a) fiber optic sensors or (b) fiber Bragg grating sensors utilize the changes in the characteristics of the light signal transmitted along the fibers that are implanted into concrete to detect various structural parameters (such as pressure, strain, humidity, rotation, and chemistry, etc); (c) electrochemical sensors use the potential difference between two electrodes mounted on a reference and the internal steel to detect the composition or the quantity of a specific chemical element and the presence of a particular element or chemic activity; (d) as the earliest SHM technique invented in the early 1880s, piezoelectric sensors can measure variations in parameters, such as acoustic emission, temperature, strain, force, pressure, or acceleration, and further detect the structural criteria [27].

The above four solutions are *intrusive* because they require *cables* to connect the embedded sensors in the concrete. They all suffer from the inconvenience of wired connections for power supply and/or data acquisition and the high costs. Moreover, the monitoring is only taken in a very limited region where the cable can reach, with a small number of sensors. This scenario hinders SHM from being more widely adopted as a ubiquitous function for civilian buildings. Instead, the existing solutions are mainly employed for

---

SIGCOMM '22, August 22–26, 2022, Amsterdam, Netherlands

ACM ISBN 978-1-4503-9420-8/22/08…$15.00
https://doi.org/10.1145/3544216.3544270

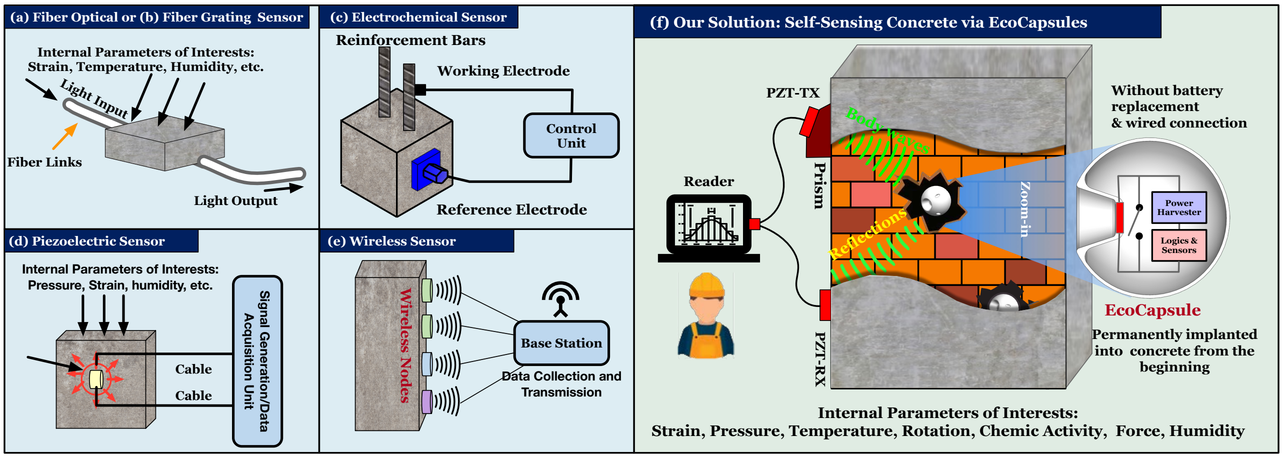

Fig. 1: Sensing Solutions for SHM. (a) - (e) shows the traditional sensing solutions by using fiber optical or fiber grating sensors, electrochemical sensors, piezoelectric sensors and wireless sensors; (f) shows our solution where EcoCapsules are mixed into concrete when the walls are being built. Afterwards, the operator can intrusively attach the transmitting and receiving PZTs onto the wall to communicate with the EcoCapsules implanted early, thereby acquiring the SHM-related data from the sensors integrated within the EcoCapsules.

highly expensive major infrastructures (e.g., bridges or skyscrapers).

The RF-based wireless sensor network (WSN) was introduced as a promising alternative solution [44] dissolving cable bonds. However, the WSN is still rarely employed for SHM in practice because of two main reasons. The battery-driven sensor node must be updated regularly for battery replacement. Such behaviour may either harm the building or constrain the deployment of sensors. Second, the reinforced concrete is made by mixing sand, water, and steel, which form a natural Faraday cage preventing from the inside RF signals out or vice versa. Thus, WSN nodes are only attached on the surface of a building, as shown in Fig. 1(e), thereby failing to meet the demand of internal structure monitoring, which is more valuable than the superficial traits monitoring. In recent years, architecture experts envision a type of self-sensing concrete by mixing minor functional fillers into the conventional concrete. The presence of these functional fillers provides the concrete to have an interchangeable and sensible wireless network from outside.

In this work, we push this vision forward by introducing a battery-free, computable, sensible and connectable filler, called EcoCapsule. This pint-sized and cost-effective piezoelectric backscatter sensor can be wirelessly charged and connected via elastic mechanical waves. As part of the concrete, EcoCapsule nodes are mixed with cement, sands, waters, and other raw materials during building construction. They can be implanted permanently into a building without follow-up maintenance, thereby ensuring the structural intact of the target building during the running period. As shown in Fig. 1 (f), when acquiring structural parameters of interests (e.g., strain, acceleration, etc), the operators attach the transmitting and receiving piezoelectric transducers (PZTs) on the surface, which exert well-designed elastic waves into the concrete to power up EcoCapsules for sensing and communication. Afterward, EcoCapsules send back data by using the backscatter communication, i.e., reflecting or not reflecting elastic wave to modulate bit one or zero.

Piezoelectric backscatter systems (PBSs) have been successfully applied to underwater communication [31, 36]. However, whether they are applicable to a concrete environment (soli media) remains unclear. In particular, applying a PBS for wireless communication in solid materials entails three main challenges.

- First, the fundamental challenge is that the propagation of mechanical waves (i.e., elastic waves) in solid materials (e.g., concrete) is much more complicated than that in liquid materials (e.g., air or water). In particular, an elastic wave travels in liquid materials with a *single* mode. On the contrary, five or above multiple modes are activated, traveling in solid materials. In short, different wave modes can be regarded as multiple copies of the original elastic wave, but they travel with different physical forms and speeds. The coexistence of these copies eventually results in severe intra-symbol interference at the receiver side (i.e., EcoCapsule), degrading the efficiency of energy harvesting and symbol decoding. We first characterize the signal propagation in concrete and then design a *wave prism* to deal with the issue mentioned by eliminating redundant modes but maintaining the S-wave as the single carrier.
- Second, the reader modulates bit one or zero through the PIE encoded on/off keying (OOK) in the downlink; that is, turning on or off the transmitting PZT. Nevertheless, a PZT still vibrates even after the driving voltage is turned off because of the inertia (i.e., ring effect), resulting in serious bit tailing and further intersymbol interference. We take advantage of the resonance effect and dual-frequency based FSK to achieve the OOK at the receiver side. In particular, the PZT is vibrated at a resonant or non-resonant frequency of the concrete (rather than turning it on or off). The concrete naturally suppresses the waves at non-resonant frequency because of the off-resonance. EcoCapsule nodes eventually receive the high/low amplitude bits similar to the OOK encoded bits.
- Finally, the external pressure that an EcoCapsule receives from the surrounding concrete is approximately 2.4× higher than that from underwater in the same depth. We design spherical and stressless shells to overcome such harsh deployment environment for protecting the internal circuity from being cracked or deformed. We also add an array of Helmholtz resonators in the front of the receiving PZT at an EcoCapsule to amplify the arrived waves further.

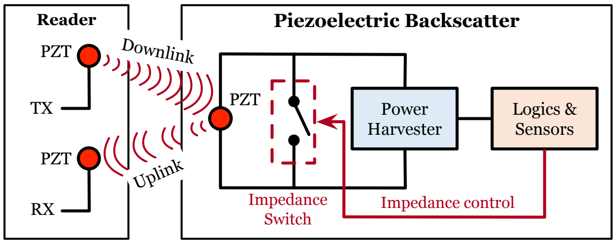

Fig. 2: Illustration of a PBS. An EcoCapsule communicates bits of zero and one by controlling the piezoelectric impedance switch, making the node either in absorptive or in reflective states.

Summary of Results. We prototype dozens of EcoCapsules. Each consists of a mechanically fabricated PZT, a Helmholtz resonator array (HRA), and a custom-made motherboard that incorporates the energy harvesting unit, a microcontroller, and an extensible peripheral interface that integrates with various sensors (e.g., strain, temperature, and humanity sensors). Our results demonstrate that EcoCapsule implanted into real-life concrete can be successfully powered up and wirelessly connected through the continuous body waves (CBW). We can achieve a maximum power-up range of more than 6 m and a throughput of up to 13 kbps. We also demonstrate that EcoCapsules can be implanted into various types of concrete, including the ultra-high-performance fiber-reinforced concrete (UHPFRC), whose compressive strength is up to 215 MPa, thanks to the stressless shell design. Finally, we demonstrate a pilot study on the structural health monitoring of a real-life footbridge over 17 months.

Contributions: In this study, backscatter systems are deployed into concrete for wireless charging, communication, and sensing. We collaborate with experts from the field of civil engineering to successfully address a long-standing problem that has puzzled the SHM for decades. This work also contributes to a prototype implementation and a long-term pilot study.

2 BACKGROUND

Piezoelectricity was discovered by Curie Brothers in 1880. It is a process in which certain types of crystals can generate an electric charge from a mechanical deformation or vice versa. Piezoelectricity has been widely used in various applications, including Quartz clocks, buzzers, inkjet printers, and X-ray shutters. A piezoelectric transducer (PZT) can convert mechanical waves (e.g., ultrasonic signals) into electrical signals at the same frequency by taking advantage of piezoelectricity. Alternatively, it starts to vibrate and further produce ultrasonic signals when exerted by an alternative electrical charge on its two terminals. In short, a PZT responds to both electrical and mechanical stimuli.

A piezoelectric backscatter system (PBS) leverages the piezoelectricity effect to achieve a battery-free wireless network based on backscatter-based communication. Similar to an RF backscatter system, a PBS consists of two main components, a reader (in analogy to RFID reader) and backscatter nodes (in analogy to RFID tags), as shown in Fig. 2. The reader contains two PZTs. One (i.e., TX) is used to generate a continuous ultrasonic wave, whereas the other (i.e., RX) aims to collect the response from a backscatter. A typical piezoelectric backscatter node comprises a single PZT, an impedance switch, a power harvesting unit, and logic and sensor circuitry. The switch is controlled by the backscatter's logic, resulting in two states, absorptive or reflective. In a backscatter node, the switch is turned off by default. Thus, the backscatter holds in the absorptive state to harvest as much power as possible until the MCU is activated. When the backscatter is powered up, both sides can start to communicate with each other through two links: downlink and uplink. The downlink is from the reader to the backscatter, whereas the uplink is reversed. In the uplink, the backscatter toggles between the absorptive and reflective states to modulate bit zero and bit one. Acting as a mirror, the backscatter node uses its PZT to reflect or not reflect signals and achieve a simple OOK-based communication.

3 WIRELESS CHARGING AND WIRELESS COMMUNICATION IN CONCRETE

The PBS is introduced into the interior of solid materials for the first time. To do so, we start by introducing the characteristics of our wireless media and then address three fundamental issues in this section.

3.1 Wireless Media: Elastic Waves

An elastic wave generally travels through a solid or fluid material or surface without causing permanent structural or physical changes. Elastic waves appear in various forms with different characteristics. They are generally classified into two types: body wave and surface wave. As the name suggests, the body wave travels through the interior of the media, whereas surface wave only moves along the surface. In this regard, we focus on body waves in this study because EcoCapsule is deployed deep into the concrete.

Body waves travel in three dimensions and can move through the interior of the solid media. In particular, body waves have two modes (as Fig. 23 shows in Appendix. A). The first mode of body wave is called the primary wave, referred to as P-wave. P-waves alternatively push or pull the media as it moves through it when spreading out. P-waves can travel through both solid rock and liquid materials at different velocities depending on the material through which they move. The second mode of body wave is called the secondary wave, referred to as S-waves. S-wave is a transverse waveform that shears the ground sideways at right angles to the direction of travel. Shearing or twisting a liquid is impossible. Thus, S-waves do not exist underwater, making underwater PBS relatively easier to achieve.

The two modes of body waves can be simply regarded as two copies of the input wave, traveling with two different waveforms and velocities. Particularly, S-waves are typically 40% slower than P-waves in a solid material. For example, $C_p \approx 3338m/s$ and $C_s \approx 1941m/s$ where C_p and C_s are the velocities of P-wave and S-wave in concrete, respectively [41]. In addition, the attenuation coefficient of S-wave is much smaller than that of P-waves [39], which means S-wave can travel further than P-wave. Notably, S-wave is preferable as the wireless media for our purpose regarding the range.

3.2 Wireless Charging

Providing power to EcoCapsules unremittingly, the reader injects a continuous body wave (CBW) into the region of interest, such

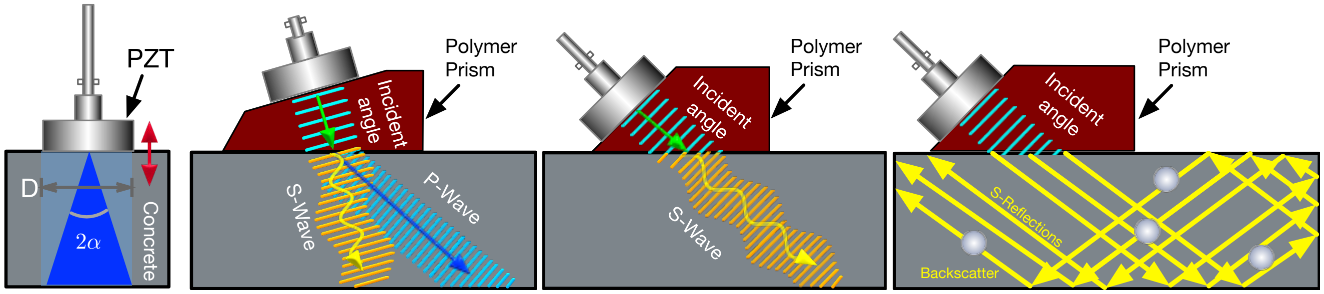

(a) 0° incidence (b) 15° incidence (c) 40° incidence (d) Wireless charging with S-reflections

Fig. 3: Injecting elastic waves into concrete with different means. (a) Transmission of body wave at a perpendicular plane boundary. (b) Both modes of body wave exist in the wall when the incident angle is less than the critical angle; (c) When the incident angle is beyond the critical angle, the P-wave no longer exists, and all refracted energy is contained in the S-wave. (d) The S-waves are reflected off the boundaries to create many reflections called S-reflections.

as a wall. The transmitting PZT of the reader is a piezoelectric round disc. It can vibrate along the direction perpendicular to the disc (i.e., in a push-pull pattern) but cannot vibrate upwards and downwards (i.e., in an up-and-down pattern). Thus, a PZT can generate P-waves only. When a PZT is attached to a wall directly, the generated P-waves travel through the wall until encounter the surface on the other side. The half-beam angle α of the P-wave can be computed as $\alpha = \arcsin(0.514C_p/fD)$ where D is the diameter of the PZT, f is the frequency, and C_p is the velocity of the P-wave in the concrete. Given that $D = 40$ mm and $f = 230$ kHz, then $\alpha \approx 11°$. The generated CBW can only cover a 132 cm^3 small cone with regard to the 15 cm concrete, as shown in Fig. 3(a). Only the nodes right under the PZT can be powered up. Even worse, the locations of EcoCapsules inside concrete are unknown. This scenario requires us to exhaustively search the whole wall area in the hope of accidentally waking up backscatter, which is obviously not a viable approach.

Reflection. *Thus, how can we power up multiple backscatter nodes inside a wall using a single transmitting PZT and without knowing their locations?* We notice that body waves bounce off when they encounter a boundary between two dissimilar mediums, such as the concrete and the air. The reflection coefficient is computed as:

$$R = \frac{Z_{\text{con}} - Z_{\text{air}}}{Z_{\text{con}} + Z_{\text{air}}} \tag{1}$$

where Z_{con} and Z_{air} are the acoustic impedance for the concrete and the air, respectively. According to the report [61], $Z_{\text{con}} = 4.66\times10^6$ kg/m^{2}s and $Z_{\text{air}} = 4.15\times10^2$ kg/m^{2}s. The high impedance differences $Z_{\text{con}} \gg Z_{\text{air}}$ result in a reflection coefficient of nearly 100%, i.e., $R = 99.98\%$, that is, more than 99% of the body waves inside concrete entirely bounce off the boundary. This phenomenon inspires us to increase the coverage by internal reflections. Therefore, we inject the body waves at a non-zero incident angle using a polymer wedge called *wave prism*, which is placed between the PZT and the concrete surface, as shown in Fig. 3(b). We can adjust the inclined plane of the prism to inject body waves from different incident angles. In this way, the P-waves generated by the PZT attached to the inclined plane are conducted into the concrete via the prism. Ideally, these waves will be bounced off the boundaries many times until the entire interior is filled with the reflections, as shown in Fig. 3(d), charging the backscatter nodes at arbitrary positions with zero effort.

However, when P-waves generated by the PZT go across the boundary between the prism and the concrete, part of their energy continues to go forward as a P-wave, whereas the other part is converted into an S-wave that begins to propagate. Thus, two modes of body waves are eventually present in the concrete, i.e., *one mode in two modes out*, as shown in Fig. 3(b). A receiving PZT cannot tell which kind of wave is received. Both mode waves will induce indistinguishable mechanical vibrations on the PZT, leading to difficulty in decoding a superposition of two copies of identical data, which are piggybacked by the P-wave and S-wave, In particular, the 60% data overlap because the S-wave spreads 40% slower than P-wave, as mentioned.

Refraction. The Snell's law suggests that a wave is *refracted* when it travels through a boundary between two different materials at a non-zero angle, and the refraction angle is computed as:

$$\frac{\sin\theta_i}{C_i} = \frac{\sin\theta_p}{C_p} = \frac{\sin\theta_s}{C_s} \tag{2}$$

where θ_i and C_i are the incident angle and the wave velocity in the first material, θ_p (or θ_s) and C_p (or C_s) are the refracted angle and the velocity of the P-wave (or S-wave) in the second material, i.e., $\theta_i, \theta_p, \theta_s \in [0, 90°]$. As mentioned, P-wave travels 40% faster than S-wave. On the basis of the above equation, we obtain the following:

$$C_p > C_s \Longrightarrow \theta_p > \theta_s \tag{3}$$

The above inequality suggests that the refracted angle of the P-wave is larger than that of the S-wave, as illustrated in 3(b). Both refracted angles are increased as the incident angle increases [12]. As a result, the refracted angle of the P-wave reaches 90° when the incident angle is increased to the first critical angle. In this case, the P-wave disappears but the S-wave still resides in the concrete. If we continue to increase the incident angle to the second critical angle, the S-wave disappears, and no body waves present in concrete. We plot the relative amplitudes of the two wave modes as a function of the incident angle in Fig. 4. The first and second critical angles are approximately 34° and 73° respectively, between which only S-wave resides in the concrete. Thus, we should inject the wave at an incident angle $\theta_i \in [34°, 73°]$ to trigger reflections of S-wave (called S-reflections) only in the broader area, as shown Fig. 3(d). In this way, the P-wave can be eliminated, and meanwhile an EcoCapsule at the arbitrary position can be wirelessly charged via S-reflections.

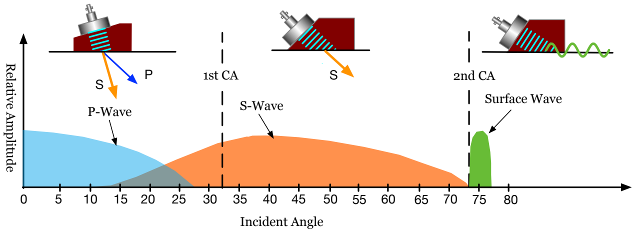

Fig. 4: Relative amplitudes of P and S waves vs. incident angle. The P- and S-waves dominate the body alternatively as a function of the incident angle. Beyond the first critical angle (CA), the P-wave disappears and only S-wave resides. Beyond the second critical angle, two models of waves disappear and no body waves present inside the concrete.

There is a trade-off when choosing the appropriate materials to fabricate the wave prism. On the one hand, the sound speed in the prism must be far less than that in concrete such that the refracted wave can be easily eliminated with a smaller incident angle. On the other hand, we hope the sound speed of the prism is sufficiently large such that the impedance difference between the prism and concrete is as small as possible, enabling more energy to be conducted into the concrete through the prism (see Eqn. 1, where the impedance is computed as the product of sound velocity and material density). We choose polylactic acid (PLA) as the material for the prism, whose density is a half of the concrete (i.e., $C_{\text{prism}} \approx 1250\ \text{m/s}^2$ and $C_{\text{con}} \approx 3700\ \text{m/s}^2$). The reflection coefficient $R \approx 33.43\%$ (i.e., approximately 67% energy of P-waves generated by the PZT can be conducted into the concrete), and the first critical angle is lowered to 34°. PLA has a high universality due to the small difference in sound velocity in different concrete. That is, we do not need to change the material of the prism to adapt to different concretes.

3.3 Wireless Communication: Downlink

The downlink is the from the reader to backscatters with two purposes, energy supply and command delivery.

Concrete Frequency Response. *Which vibrating frequency benefits the propagation of body wave inside concrete the most?* We conduct several experiments to answer this question by measuring the concrete frequency response, which is a quantitative measurement of the output spectrum of concrete in response to a stimulus. Nowadays, the majority of the modern buildings are constructed with three typical concrete blocks made from different materials, including normal concrete (NC) [63], ultra-high performance concrete (UHPC) [28], and ultra-high-performance fiber-reinforced concrete (UHPFRC) [57]. We test four concrete blocks, 7 cm-thick NC, 15 cm-thick NC, 15 cm-UHPC and 15 cm-thick UHPFRC, as shown in Fig. 5(a). Their detailed mix proportions and physical properties are listed in Table 1 (see Appendix. B). They are 15 cm wide and 15 cm high. In each experiment, we attach a transmitting PZT with a 45° prism on one side of a concrete block and attach the receiving PZT on the other side. The surface waves are almost filtered out because of the sharp edges and corners. The working frequencies of the two PZTs range from 1 kHz to 1 MHz. We transmit a sinusoidal signal at a frequency through the transmitting PZT each time. The peak voltage is 100 V. We sweep the working frequency from 20 kHz to 400 kHz with a step of 10 kHz. For each setting, we performed ten trials and reported the average. The results are plotted in Fig. 5(b). We obtain two important findings from the figure. First, regardless of concrete type, the resonate frequency appears between 200 kHz and 250 kHz, beyond which the propagation attenuates rapidly. Second, the peak responses of UHPC and UHPFRC concrete are far greater than the peak response of NC because the former has larger compressive strengths and less intermolecular distances than the latter, thereby benefiting the propagation of elastic waves.

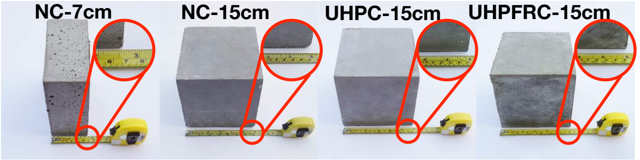

(a) Tested concrete blocks

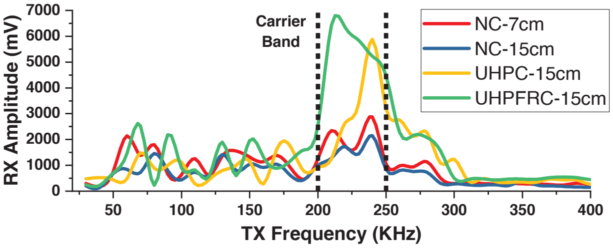

(b) Frequency response

Fig. 5: Concrete Frequency Response. We collected the the responses of four morden concrete blocks to the vibrating stimuli at various frequencies.

Pulse Interval Encoding (PIE). We adopt PIE, a commonly used data coding scheme for downlink transmissions in backscatter systems. As shown in Fig. 6, a bit zero is coded as a shorter high-voltage interval with the same low-voltage pulse, and a bit one is coded as a short low-voltage pulse following a long high-voltage interval. The PIE scheme is preferred in battery-free networks, where it ensures that at least 50% of the maximum power is delivered to the backscatter even when the transmitted data contains long strings of zeros by using equal low and high voltage for a bit zero. If the high voltage is three times as long as the low voltage for a bit zero, a random stream of equally mixed binary data provides approximately 63% of peak power. Consequently, the backscatter node can always harvest energy from the CBW even if commands are piggybacked.

Ring Effect. Ideally, the wave should be completely limited within the high-voltage edge in a PIE symbol to avoid interference to the following low-voltage edge (i.e., intra-symbol interference), as shown in Fig. 6. However, in practice, the PZT still vibrates even after the driver stops the vibration, leading to a long tail, which is known as the *ring effect*, caused by the inertia, i.e., the PZT continues to oscillate for a certain period after the driving voltage is turned off [49]. The symbol may be incorrectly demodulated because of the high-ended tailing noise. Fig. 7(a) shows a symbol of bit zero, where the symbol lasts from 0.1 ms to 1.1 ms, and the transition occurs at 0.6 ms. Although the power is off at the transition point, the vibration dampens slowly and consumes an additional 0.3 ms to overcome the moving inertia. The traditional approach of the

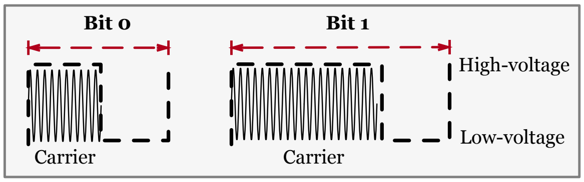

Fig. 6: Illustration of PIE symbols in baseband. Both symbols are composed a high-voltage edge and a low-voltage edge to ensure that a backscatter can harvest energy during at least 50% time.

anti-ring-effect is to apply a reverse braking voltage in the ending of the high-power edge to counteract the tailing wave. However, this approach encounters two difficulties, that is, the parameters of braking timing and braking voltage are hard to determine. Braking too early or too late (braking too high or too low) weakens the ending of the high-voltage edge or raises the beginning of the low-voltage edge.

FSK in OOK out. As mentioned, the CBW responds with a higher amplitude at a resonant frequency but with a lower amplitude at a non-resonant frequency (see Fig. 5(b)). We take advantage of this feature to overcome the ring effect. We choose to adjust the PZT to vibrate at a non-resonant frequency for low-voltage edges rather than to stop the vibration completely. Specifically, the CBW is transmitted at a resonant frequency (e.g., 230 kHz) for the high-voltage edge but a non-resonant frequency (e.g., 180 kHz) for the low-voltage edge, whose amplitude is lowered down naturally by the concrete because of the non-resonant radiation damping. Starting or stopping the vibration of the PZT is not required, thereby reducing the influence of inertia. Fig. 7(b) shows the results of our anti-ring-effect approach, where the concrete effectively suppresses the tailing. Therefore, unlike the traditional backscatter system, which adopts OOK for the downlink, our trick uses frequency-shifted keying (FSK) plus the off-resonance effect to achieve OOK in the side of backscatter nodes. Notably, data can still be decoded using a simple envelope detector equipped into EcoCapsules. Thus, the power consumption and fabrication cost are minimized.

3.4 Wireless Communication: Uplink

The uplink is initiated by an EcoCapsule to transmit sensing data to the reader through the backscatter communication.

Backscatterring. We run an experiment with an EcoCapsule implanted into a 15 cm-thick UHPC block to validate the feasibility of backscatter communication in concrete. We transmit a single-tone CBW at 230 kHz with a peak voltage of 100 V to supply the energy and provide the backscatter carrier to an EcoCapsule. The EcoCapsule is programmed to turn on and off the impedance switch at a frequency of 2 kHz. We use another PZT to receive the backscattered waves and convert them into electronic signals. This receiving PZT tightly adheres to the wall without a prism. Thus, it can be viewed as a part of the concrete to receive S-reflections directly. Following the practices of traditional backscatter systems, we adopt FM0 coding schemes to increase robustness. FM0 uses the presence or absence of a transition during a symbol window to determine a bit zero or a bit one instead of the total duration. This experiment demonstrates the feasibility of the backscattering communication inside the concrete.

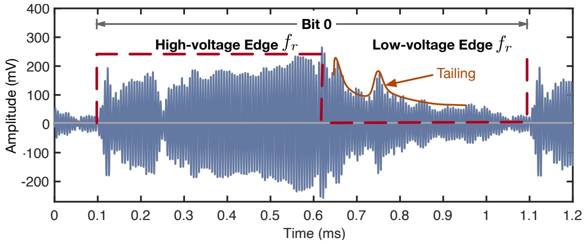

(a) Vibration tailing

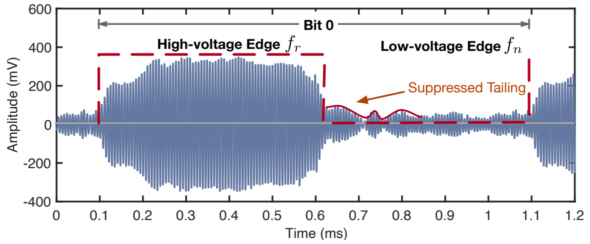

(b) Suppressed tailing

Fig. 7: Ring effect. (a) shows the PIE symbol zero without tailing suppression; (b) the tailing is suppressed by the concrete naturally due to the off-resonance effect.

Self-interference. The S-reflections and the surface waves leaked from the transmitting PZT are 10× stronger than the backscattered signals. They overwhelm the receiving PZT and prevent it from detecting weak backscatter signals. We adopt a similar solution used in RFID system [45] or previous underwater PBS [31, 36] to overcome such self-interference. In this solution, the backscatter nodes respond at a shifted backscatter link frequency (BLF), i.e., several kHz is reserved as a guard band between the downlink and the uplink. Thus, self-interference can be easily filtered out in the spectrum. For more details refer to Appendix C.

Scaling to Multiple EcoCapsules. Finally, we adopt the time division multiple access (TDMA) mechanism as used in RFID Gen 2 protocol to support multiple EcoCapsules. Each EcoCapsule randomly selects a time slot to transmit its data. The TDMA is acceptable in our scenario because a limited number of EcoCapsules are implanted into a wall. Meanwhile, SHM can tolerate a relatively longer delay because the degradation of a building takes days rather than seconds.

3.5 Practical Discussion

(1) *Acoustic vs. RF backscatter for in-concrete SHM?* There have been numerous attempts to embed passive RFID tags to implement the long-term in-concrete SHM [37, 53, 62]. They have demonstrated that the communication ranges of these RF based backscatters are limited to several centimeters when implanted into concrete because of the severe attenuations caused by the concrete. In contrast, concrete is well known as good conductors for mechanical vibrations, allowing up to meters of communication range. Thus, we believe that the PBS will become the future for in-concrete communications.

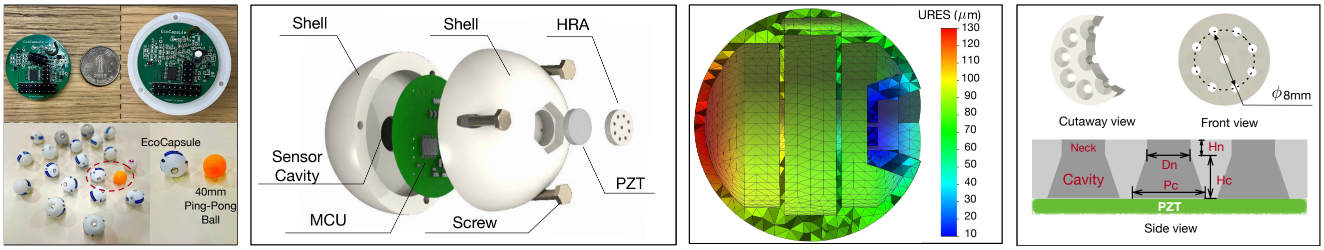

(a) EcoCapsules (b) Exploded view (c) Stress distribution (d) Helmholtz Resonator Array

Fig. 8: Mechanical and hardware fabrication. (a) shows the EcoCapsule prototypes (white) compared with a standard 40 mm ping-pong ball (yellow). Their internal circuit board is nearly as small as a one-dollar coin; (b) shows the exploded view of an EcoCapsule; (c) shows the stress distribution; (d) zooms into the HRA.

(2) *The impact of the concrete structure.* Today the internal structure of concrete is very complicated and diverse. For example, the concrete may have steel reinforcement bars, irregular sand particles, and gravel. It may also have cavities due to mixed air during the casting process [55]. These objects inside the concrete affecting the acoustic communication are analogous to the reflectors in the air on RF communication. The acoustic wave will reflect or diffract when it encounters them, resulting in changes in direction, frequency, and intensity. However, such foreign objects make up only a small portion of the concrete and cannot cause strong interference to normal communication in most cases. Moreover, our experiences indicate that fine-tuning the frequency can significantly improve the channel when the channel deteriorates due to foreign objects.

4 IMPLEMENTATION OF ECOCAPSULES

In this section, we describe our mechanical and hardware fabrication process for EcoCapsules. The detailed hardware and software design has been released on the Github [10] and our project website [5].

4.1 Stressless and Resonant Shell

Fig. 8(a) shows our fabricated EcoCapsule prototypes, which are in the shape of spheres with small sunken mouths. Each one is the size of a standard ping-pong (i.e., 4.5 cm diameter). Such design is dedicated to two purposes, stress equalization and Helmholtz resonance.

Stress Equalization. The spherical shell can help equalize the stress from the surrounding concrete. However, we still need extra effort to reinforce the structure such that it is not cracked by the concrete because of the pressure difference between the internal air and external concrete of the shell. The difference between the internal (air) and external (concrete) pressure denoted by $\Delta\mathcal{P}$ is given by:

$$\Delta\mathcal{P} = \rho g h - \mathcal{P}_{\text{air}} \tag{4}$$

where ρ is the density of the concrete, h is the height of the building, g is the gravitational acceleration, and $\mathcal{P}_{\text{air}}$ is standard atmospheric pressure (i.e., 101.325 kPa). The density usually varies from 1840 kg/cm^3 to 2360 kg/cm^3 for ordinary concrete [46]. The shell is fabricated with stereolithography (SLA) 3D printing technology, which leverages resin as the raw material. The resin used for SLA has approximately 65.0 MPa tensile strength and approximately 2.2 GPa Young's modulus [14]. The shell thickness is set to 2.0 mm, and 5% deformation is tolerated at most. We input these parameters into Solidworks [15] to figure out the maximal pressure difference that such a shell can tolerate by using the method of finite element analysis. The result shows that $\Delta\mathcal{P}_{\text{max}} \approx 4.3$ MPa. We can obtain the maximal height $h_{\text{max}} = 195$ m by substituting $\Delta\mathcal{P}_{\text{max}}$ into Eqn. 4. Thus, our current prototypes can be implanted into any building under 195 m ($\sim$ 55 floors). We can adopt metal materials to bear higher buildings, e.g., the $\Delta\mathcal{P}_{\text{max}} \approx 115.2$ MPa for the shell made from alloy steel and $h_{\text{max}} = 4985$ m, which is far higher than the highest man-made building on the Earth.

Then, we design the internal structure of the shell. In particular, the interior of the sphere is divided into three cavities by two clapboards, as shown in Fig. 8(b). The PZT with a diameter of 10 mm is attached to the end of the sunken mouth. The PZT must be exposed to concrete. Thus, the mouth benefits to protect it from being snapped off when the liquid cement is poured. The motherboard is fixed in the middle cavity between two clapboards, and the sensors are installed in the rear cavity to sense the environment within the concrete. Fig. 8(c) shows the distribution of stress exerted by the surrounding concrete, which is described by resultant displacements (URES) [20]. The designed internal structure successfully transfers the majority of pressure/stress onto the shell and the clapboards such that the electronic components receive nearly zero stress. Thus, these components are well protected from external pressure.

Helmholtz Resonance. A Helmholtz resonator (HR) is a container of moving media (such as air or concrete) with an open neck. At the Helmholtz resonance, a volume of media in and near the open neck vibrates because of the "springiness" of the media inside. Helmholtz resonator can be used as a vibration amplifier, which can receive a tiny vibration at a specific frequency and enhance it by the resonance of the cavity. Inspired by this effect, we design a Helmholtz resonator array (HRA) and deploy it in the front of the PZT, as shown in Fig. 8(b). The structures of the HRA and each HR are shown in Fig. 8(d). Each HR is composed of a neck and a cavity. The media present in the cavity can be modeled as a spring because of its compressibility and the ability to store potential energy. The undamped resonant frequency f_r is computed by:

$$f_r = \frac{C_s}{2\pi}\sqrt{\frac{3A_n}{4V_cH_n}} \tag{5}$$

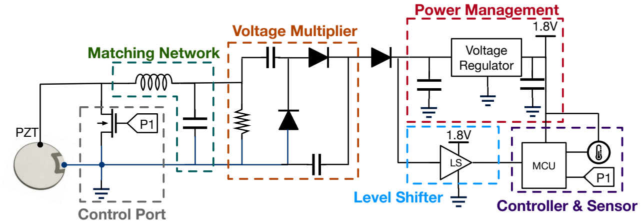

Fig. 9: Circuit schematic of EcoCapsule

where C_s is the speed of S-wave in concrete, A_n is the cross-sectional area , H_n is the length of the neck and V_c is the cavity volume. Aiming at the 230 kHz around resonant frequency, we choose the geometric parameters as follows, $A_n = 0.78$ mm^2, $V_c = 2.76$ mm^3, and $H_n = 0.8$ mm.

4.2 Circuitry

The core of EcoCapsule is a battery-free processing board, which is designed and fabricated on a round two-layer printed circuit board (PCB) (3.5 cm diameter), as shown in Fig. 8(a). It is a general-purpose and extensible computing platform for long-term SHM. Fig. 9 shows the overall schematic of our hardware design, which is inspired by WISP [43] and PAB [36]. A total of 30 prototypes are fabricated for our evaluation using the fabrication service provided by JLCPCB [7]. Each costs approximately 10 USD. The circuit components are hand-soldered on the PCBs and individually tested.

The hardware serves four purposes: power harvesting, backscatter communication (for uplink), receiving and decoding (for downlink), and interfacing with external sensors. *(1) Power Management.* The energy harvester on EcoCapsule consists of a four-stage voltage multiplier and the voltage regulator. The multiplier boosts the weak acoustic signal and converts it into a DC signal. A Ti low-dropout (LDO) regulator LP5900SD-1.8 [9] finally converts the signal into a constant 1.8V output voltage to the MCU and sensors. We add a diode in front of the LDO to prevent current from flowing back into the supply [8]. *(2) Demodulation.* The demodulator reuses the voltage multiplier as an envelope detector to extract the baseband signal. Like PAB [36], we use a level shifter TXB0302 [18] to further filter out high-frequency noises and binarize the output signal. *(3) Controller and Sensor.* We choose the Ti MSP430G2553 MCU [19] which has an ultralow-power mode, to meet our request. The MCU consumes 414 μW in active mode and 0.9 μW in sleep mode. The MCU decodes the downlink PIE command by using the timer interrupt to measure the time interval between every edge of the demodulator output [36]. We use the internal ADC pin to sample the analog sensors and use the I^{2}C protocol to communicate with digital sensors. *(4) Sensing Functions.* We tested three types of concrete internal sensing applications, temperature, humidity, and strain. To measure the internal relative humidity (IRH) and temperature, we use AHT10 Integrated temperature and humidity sensor [1]. We place a BFH1K-3EB full-bridge strain gauge [2] on the back of the node shell to measure two-directional concrete internal strains.

5 EVALUATION

This section introduces the evaluation methodology and the results.

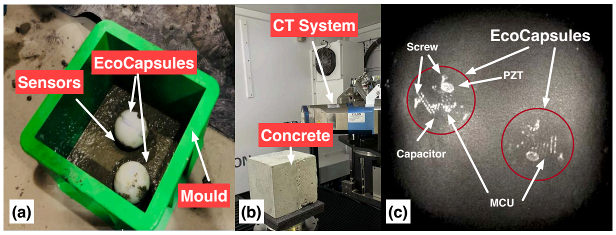

Fig. 10: Concrete production and CT examination

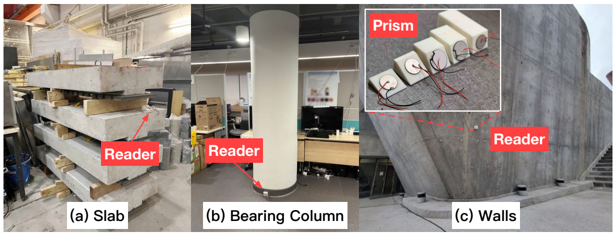

Fig. 11: Tested concrete structures and wave prisms

5.1 Methodology

First, we describe the experimental setup and methodology.

Reader. (1) *Transmitter.* The transmitter consists of a wave prism, transmitting PZT, and a frontend that converts baseband signal to PZT vibrations. In particular, the transmitting PZT is a 2 mm thick disc with a diameter of 40 mm, working at 230 kHz. We adopt such a relatively larger PZT (than the one used in a node) to withstand the highest peak voltage of 250 V. The prism is made of PLA and fabricated by 3D printing. The default incident angle is 60°. The PZT is connected to a Rigol DG2052 signal generator [13] through a Ciprian HVA-400-A power amplifier [3]. We design a matching network to optimize the power transfer between the power amplifier and the transmitting PZT. The signal generator is controlled by a Lenovo Thinkpad PC through a serial port. We use MATLAB to generate the downlink signal moduled by PIE. We design the downlink packet structure following the EPC UHF Gen2 protocol [6]. The downlink packet may include commands to set nodes' backscatter link frequencies and request their sensed data. (2) *Receiver.* The receiver is implemented using a PZT the same as the transmitting PZT but without a prism. The receiving PZT is connected to the OWON XDS3000 oscilloscope [11] to collect the signal. The sampling rate is 1 MS/s. We develop a MATLAB-based decoding program to post-process the signals. The decoder first takes a carrier frequency estimation by analyzing the power carrier and then performs a digital downconversion to extract the baseband backscatter signal. Finally, a maximum likelihood decoder is used to decode the FM0 data.

Concrete Casting: We use a standard mould to cast self-sensing concrete blocks, as shown in Fig. 10 (a). The materials and properties of the four types of concrete blocks have been introduced in Table 1 of Appendix B. These blocks are the basic units to build a house. In practice, we can also directly pour nodes into the load-bearing walls or columns in practice. Afterward, we use YXLON FF35 CT scan machine [21] to examine the structure intactness after the concrete blocks are solidified (see Fig. 10 (b)). The image result is shown in Fig. 10 (c), from which we can observe the intact shells

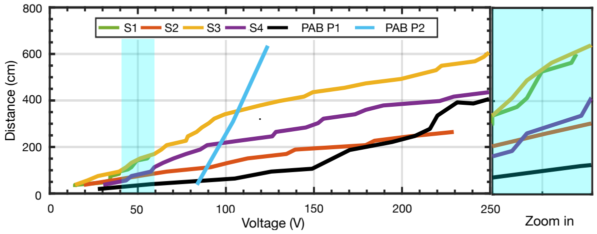

Fig. 12: Range vs. Voltage

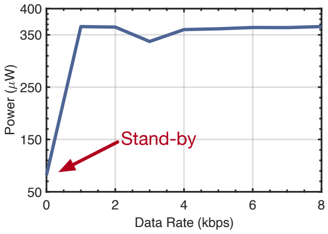

Fig. 13: Power Consumption

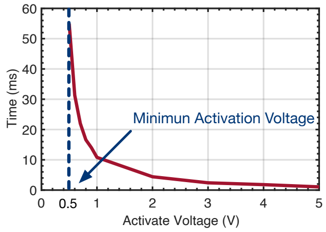

Fig. 14: Cold start

and components of the two nodes and verify the rugged structural design visually.

Experiment Settings: We adhere the constructed concrete blocks onto a building using concrete glue to avoid vandalizing the building. The glue may cause an approximately 3% loss of wave energy. The experiments are conducted on three types of concrete structures, (S1) a 150 × 50 × 15 cm concrete slab [4], (S2) a 250 cm-high load-bearing column with a 70 cm diameter, (S3) a 2000 × 2000 × 20 cm common wall, and (S4) a 2000 × 2000 × 50 cm protective wall, as shown in Fig. 11. The distance between the transmitting PZT and receiving PZT of the reader is approximately 20 cm. The distance from the nodes to the reader varies across our experimental trails. The bitrate of the uplink is set to 1 kbps, and the 60° prism is used by default unless noted. We also adopt the underwater backscatter system, PAB [36] operating at 15 kHz, as the baseline for comparison. The following evaluation is taken regarding the performance of wireless charging, the uplink, and the downlink, respectively.

5.2 Charging Performance

First, we evaluate the performance of wireless charging regarding the range and the power efficiency.

• **Maximum Range**. We evaluate the maximum range of an EcoCapsule node can be powered up regarding the four concrete structures as aforementioned (i.e., S1-S4). The reader transmitting at a configured voltage is moved away from the node on the structure until the EcoCapsule can not be powered up. The experiment is repeated at different transmitting voltages. We only report the result under 250 V (i.e., the maximum output voltage of our amplifier). The results are plotted in Fig. 12. For comparison, we also add the results of the two pools where the PAB [36] was tested. In the figure, the curves of S1 and S2 are terminated at their lengths of 150 cm and 250 cm, respectively. The range shows great diversity in different types of structures or materials. In particular, the maximum ranges are 130 cm, 56 cm, 134 cm, 60 cm, and 19 cm in S1, S2, S3, S4, and PAB Pool 1 at 50 V; the ranges are 235 cm, 500 cm, 385 cm, and 200 cm in S2, S3, S4, and PAB Pool 1 at 200 V. For PAB Pool 2, a larger voltage is required (84 V) for a short distance (23 cm). As the voltage increases, the communication distance rises by a significantly larger percentage than in other scenarios, to the point where only 125 V is needed for a PAB node 6.5 m away. We obtain three main findings: (1) High voltage leads to high transmit power, enabling the backscatter node to harvest more energy to be powered up at a longer range; (2) The range is longer in a narrow structure. Such structure helps the energy to be concentrated directionally as a directional RF antenna. The cylindrical column (S2) does not perform better than the two walls (S3 and S4) because the diameter of S2 is 70 cm, which is far higher than the thickness of the two walls (i.e., 20 cm and 50 cm). In particular, S3 and S4 are narrower than S2, benefitting the reflections of S-waves between the two sides of the walls. The same phenomenon is observed in the PAB experiments, where Pool 2 is elongated and acts as a corridor. A narrow structure allows for more reflections and multipath, facilitating energy to the deeper water; (3) In physics, the elastic wave usually propagates further in materials with higher density (e.g., concrete) rather than in materials with lower density (e.g., underwater). It is confirmed in Pool 1, but Pool 2 is an anomaly, which is likely because the excessive reflections mentioned in (2) make the energy too concentrated.

• **Power Consumption.** We then measure the power consumption of an EcoCapsule as a function of bitrate. We use the Ti MSP-FET hardware programming tool with EnergyTrace technology [17] to measure the power consumption of the chip and peripherals. The results are shown in Fig. 13, where the bitrate varies from 0 kbps to 8 kbps. The node is in standby mode (i.e., waiting to receive and decode the downlink signal) when the bitrate is zero. We let the MCU work at the low power mode (LMP3) when it is on standby. The node consumes only 80.1 μW in standby mode because of the excellent power performance of MSP430 and other time-saving components adopted for the circuitry. Then, the total power consumption fluctuates around 360 μW slightly regardless of the bitrate.

• **Cold Start.** In the beginning, each EcoCapsule node should take a relatively long time to activate the MCU. This process is called *cold start*, after which the reader can then initiate to broadcast commands. We use an oscilloscope to measure the time taken on the cold start. The results are plotted in Fig. 14. It can be seen that 500 mV is the minimum voltage required to activate the MCU, where the activation takes approximately 55 ms. However, the time for the cold start is rapidly decreased to 4.4 ms when the voltage is given by 2 V or above.

5.3 Uplink Performance

We explore the uplink performance of EcoCapsules using the NC block as follows:

• **BER vs. SNR**. Fig. 15 shows the bit error rate (BER) in log-scale as a function of the SNR, which is tuned by decreasing the input peak voltage at the transmitting PZT of the reader. The BER is computed as the fraction of correctly decoded bits to the total transmitted bits from the EcoCapsule node. Both underwater and in-concrete piezoelectric backscatter systems show a similar trend;

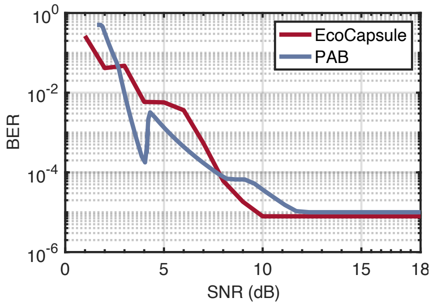

Fig. 15: BER vs. SNR

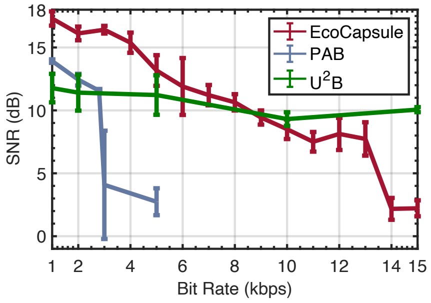

Fig. 16: SNR vs Bitrate

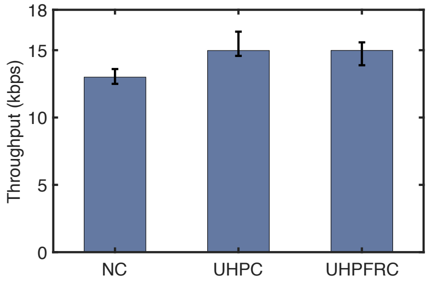

Fig. 17: Throughputs

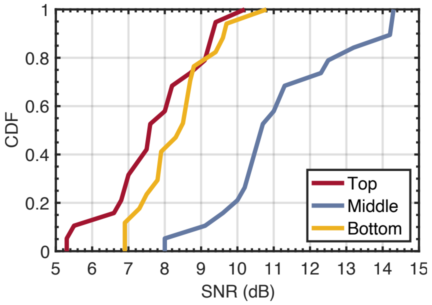

Fig. 18: SNR vs. position

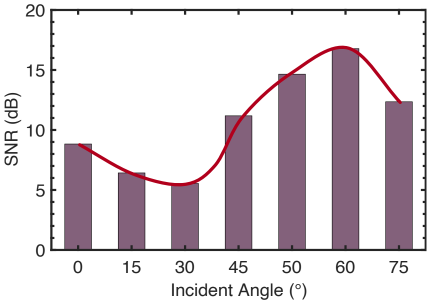

Fig. 19: Effect of prism

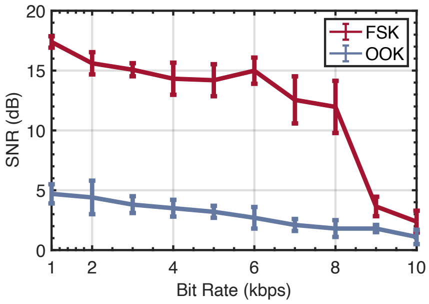

Fig. 20: SNR vs. modulation

that is, the BER decreases with an increasing SNR. The reader can tolerate a minimum SNR of approximately 2 dB, where the BER is nearly 0.5. The BER drops to the minimum of 10^{-5} at SNRs higher than 8 dB, which is comparable with the 11 dB of PAB. The result aligns with the efficiency of the FM0 coding scheme.

- **SNR vs. Bitrate**. The SNR is also highly related to the bitrate of the uplink. A higher bitrate leads to a larger bandwidth and a smaller symbol window, which may cause decoding difficulty. We aim to understand the impact of the bitrate on SNR of an *uplink signal*. Thus, we vary the bitrates from 1 kbps to 15 kbps by configuring different MCU clocks. In each setting, 10 trials are repeated. The average SNRs with standard deviations are plotted in Fig. 16. The SNR of the EcoCapsule drops rapidly to 3 dB when the bitrate exceeds 13 kbps, whereas it is limited to 3 kbps in PAB. This outperformance is derived from the benefit of adopting a higher carrier frequency (i.e., 230 kHz) in EcoCapsule. A carrier with a higher frequency can piggyback a wider data band than that with a lower frequency. Another underwater backscatter system, U^2B [31], achieves higher SNR than EcoCapsule when bitrate exceeds 9 kbps since it takes a wider band.

- **Throughput vs. Concrete.** Then, we evaluate how the material of concrete affects the uplink performance. Thus, we measure the throughputs of EcoCapsules that are implanted into three types of 15 cm concrete blocks made of NC, UHPC, and UHPFRC, respectively (see Fig. 5(a)). The results are plotted in Fig. 17. Throughput is defined as the number of bits correctly decoded by the reader per second. The resulting throughputs are all more than 13 kbps with a 2 kbps deviation. As mentioned early, high density (i.e., high compressive strength) results in a high impedance, thereby benefiting the propagation of elastic waves. This hypothesis is verified in our experiment; that is, the throughputs in UHPFRC and UHPC are about 2 kbps higher than that in NC.

- **SNR vs. Position.** Finally, we evaluate the impact of EcoCapsules positions on the channel quality. In the experiment, we glue the NC block with implanted nodes close to the wall's top margin, middle, and bottom margin. The distances between the reader and the node are similar. Fig. 18 shows the CDFs of SNR in these three areas. The EcoCapsules deployed close to the margins achieve relatively higher SNR (i.e., 11 dB and 8 dB) than those deployed in the middle (i.e., 7 dB). This is because S-waves are reflected at the margins, which benefits the nodes to harvest more power. *Surely, the reflection is a double-edged sword. Providing more power might also introduce serious self-interference to decoding at EcoCapsules. In this case, we should change the positions of transmitting TX of the reader to untie the deconstructive superposition due to the reflections.*

5.4 Downlink Performance

Finally, we evaluate the downlink performance regarding prism effectiveness and modulation scheme. In the experiments, the transmitting PZT with the prism and the receiving PZT were stuck onto the inside and outside sides of a 15 cm wall (for excluding the interference from surface waves). The TX and the RX are distanced by about 1 m. Then, we use the TX to transmit a PIE-based signal and use the RX to measure the SNR of the received downlink signal. No EcoCapsule nodes are used in this experiment to eliminate their uncertainty.

- **Prism Effectiveness**. Fig. 11(c) shows the wave prisms with different incident planes tested in this experiment. The results are shown Fig. 19. As desired, the SNR reaches the maximum of 15 dB around at 50° and 70° incident angles, which are in line with the

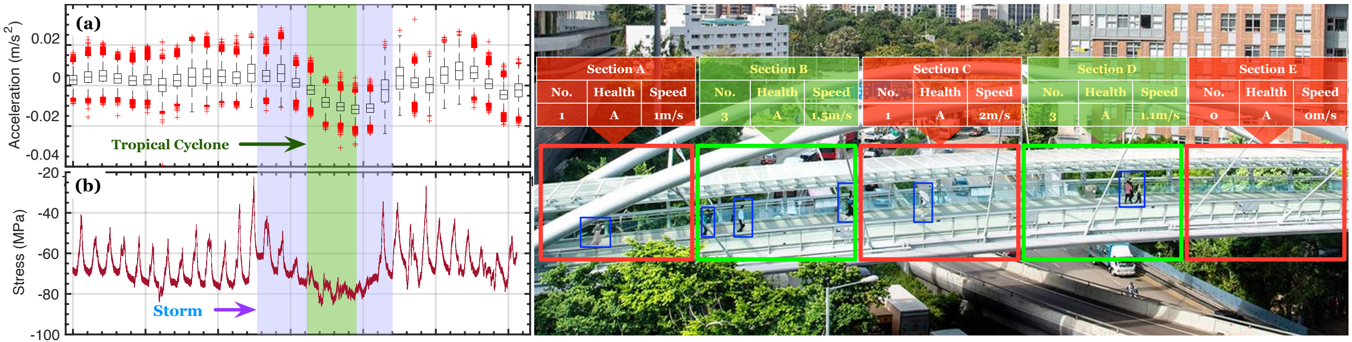

(C) Real-time health monitoring of the bridge in four sections

Fig. 21: A pilot study of real-time SHM on a footbridge. (a) and (b) shows the collected acceleration and stress measurements in July 2021. The sign of the data depends on the posture of the sensor; (c) shows the picture of the footbridge and the real-time analysis results of bridge health regarding different sections.

previous theoretical results (i.e., [34°, 73°]). The SNR drops by 73% and 30% at 15° and 30° respectively, because of the coexistence of the two wave modes. A relatively higher SNR is observed at a 0° incident angle. The reason is that we directly adhere the transmitting PZT onto the wall without a prism to achieve 0° incidence. In this case, only P-waves are injected into the wall without triggering the S-waves. This experiment demonstrates that the prism effectively improves the SNR by 30 ∼ 70%.

- **Anti-ring-effect**. Finally, we evaluate the effect of the anti-ring-effect approach, in which the transmitting PZT uses FSK to transmit PIE encoded bits, whereas the receiving PZT still receives the bits using OOK. Fig. 20 shows the SNR of the received downlink signals as a function of the bitrate. The SNR of the FSK approach is improved by about 3 ∼ 5× than the traditional OOK approach because FSK utilizes the off-resonance effect to suppress the tailing.

6 PILOT STUDY: LONG-TERM SHM OF A REAL-LIFE FOOTBRIDGE

We have been taking a pilot study on long-term structural health monitoring of a real-life footbridge since October 2019. Fig. 25 shows the structure of the footbridge [59]. The footbridge links two large-area two campuses. The bridge has a total length of 84.24 m, consisting of a 64.26 m-long main span that straddles the highway underneath and a 19.98 m-long side span. The bridge deck is constructed with two butterfly-shaped steel tube arches and two crossing columns. The maximum vertical acceleration and lateral acceleration of the bridge deck are not exceeded 0.7 m/s^2 and 0.15 m/s^2, respectively. The maximum strength of steelwork is 355 MPa. The limitation of deflection at mid-span is 0.1083 m. The maximum average pedestrian area occupancy must be less than 1 m^2/ped. Once these structural thresholds are exceeded, the whole bridge must be damaged or even collapsed. To conduct the SHM, 88 conventional SHM sensors of 13 types are installed on the bridge, as shown in Fig. 25. Fig. 21 (a) and (b) shows the samples of the two kinds of measurements (i.e., acceleration and stress) during July 2021. Particularly, we observe the exceptions during the window from 15th to 23rd July when the city experienced almost one-week-long stormy and tropical weather according to the records of the astronomical observatory. The similar patterns shown in the two data types mutually verify that the two sensors are running functionally. More sensing data are exhibited in Appendix D.

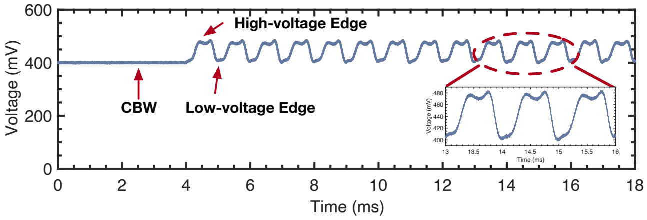

Fig. 22: Received and demodulated backscatter signal.

Many structural health criteria are defined. Here, we demonstrate to use the pedestrian area occupied (denoted by H in the unit of m^2 per pedestrian) to quantify the bridge health. As listed in Table 2 in Appx. D, the health can be graded into six levels from A to F [40]. Specifically, when $H > 2$, the bridge is in good health; when $H \leq 2$, the bridge is too crowded and might receive structural damage; when $H \leq 1$, the bridge is overloaded and will collapse. The CCTV is not sufficient to count the number of pedestrians due to the interference from blockage, insufficient lights, bad weather conditionetc. Thus, we jointly use the measurements (including acceleration, stress, displacement, etc) from all sensors and the CCTV to compute H. . Fig. 21 (c) shows the picture of the bridge and an example of the analysis results of the bridge health regarding the five sections. As a result, the bridge health always remained at B or above levels in the past year. This is mainly attributed to the public policy of social distancing against the COVID-19 pandemic.

The conventional sensors totally cost over 10 M USD, and they collect external structural parameters only. Nevertheless, our EcoCapsule sensors cost less than 1K USD totally and are the sole ones that can measure the acceleration and stress from inside. To validate their functionalities, we deployed five EcoCapsules on the concrete for preliminary tests. Since EcoCapsules are supposed to be implanted into the bridge, they do not receive the negative influence from the weather conditions or man-made interference. Therefore, they are more trustworthy than conventional sensors and benefit from reducing false positives. Fig. 22 plots the received and demodulated baseband signal. The EcoCapsule starts to backscatter from 4 ms. In the following, a standard square signal comprises two alternative amplitudes caused by the impedance switch. Each of the high- and low-voltage edges takes 0.5 ms. It can be seen that the reader can successfully establish communication with the EcoCapsule when placed inside the concrete. This study verifies that EcoCapsules can work as well as the conventional ones for the long-term monitoring but at a lower price. In the future, we will continue to conduct more structural analysis in sophisticated cases using EcoCapsules.

7 RELATED WORK

Our work is related to prior works in the following fields:

(1) Acoustic communication and sensing: Acoustic wave has been widely used to transmit data or sense around in air [38, 42], solid [26, 30, 34, 50, 52, 58, 67], and water [24, 36] to overcome the physical barriers that impede traditional wired or RF communication methods. Due to power and data transmission limitations, past solid acoustic systems have to deploy the acoustic transceivers on object surface [30, 34, 47] or inject the wired transceivers damagingly into the objects like concrete [52]. The EcoCapsule breaks this stereotype and first implants the battery-free sensors into the concrete and enables the solid wireless connection with ultra-low power consumption.

(2) Backscatter systems: Backscatter technology has gained significant attention in the wireless community. Recent works demonstrated the ability to backscatter and harvest energy from RF signal [35, 43, 48], light [60], magnetic field [64] and acoustic wave [31, 36]. The application of backscatter systems includes over-the-air connection [43], underwater exploration [31, 36] and in-body communications [51]. EcoCapsule leverages the knowledge from these past works but differs in the following aspects. First, none of the past systems was designed to work in solid-state materials. Second, in EcoCapsule, we must overcome the challenges in wireless charging and communication caused by the multiple modes of elastic waves. Last, we also must consider the structural issues due to the harsh operating environment.

(3) Structural health monitoring: Finally, our work is related to a large body of research on structural health monitoring [22, 23, 66]. SHM systems can broadly be divided into three categories: surface-mounted sensors, intrusive wired sensors, and wireless-connected embedded sensors. The surface-mounted sensors monitor the structure health by using the RF Radar [65], electrical signal [54] and acoustic wave [67]. Although they are non-destructive, the accuracy is limited, and they cannot sense slight internal variations such as strain and humidity. Intrusive wired sensing systems ensure accuracy by directly measuring the embedded sensors [32] or internal smart materials [29, 33]. However, such methods degrade the structural integrity, which can not be deployed in the real world. Recent works attempt to deploy the RF-connected sensors [25, 37, 53] to solve the SHM dilemma. However, they have a very limited communication range due to the strong attenuation of the RF signal in concrete. Additionally, the RF antenna makes its size too large to be implanted. EcoCapsule provides a novel solution to SHM by enabling solid backscatter communication. It makes SHM more accurate, flexible, and scalable.

8 CONCLUSION

In summary, we present a revolutionary structural health monitoring technology, EcoCapsule, a battery-free pint-sized sensor implanted in civilian buildings as a part of the concrete. EcoCapsules leverage body waves for wireless charging and backscatter communication. We believe this study will greatly promote the development of self-sensing concrete in the field of civil engineering. However, the size of the current prototype is still relatively larger than that of other materials of concrete, such as sands and stones. Whether mixing a large number of EcoCapsules into the concrete brings structural risks to high-rise buildings, in the long run, is unclear. In the future, we plan to transfer all logic circuity into a nano-scale chip to reduce the size to mm-scale.

Claim: This work does not raise any ethical concerns.

9 ACKNOWLEDGEMENTS

We thank all anonymous reviewers for the insightful feedback. This study is supported by NSFC Excellent Young Scientists Fund (Hong Kong and Macau) (No. 62022003), NSFC Key Program (No. 61932017), NSFC General Program (No. 61972331), UGC/GRF (No. 15204820, 15215421), and National Key R&D Program of China 2019YFB2103000. Zhenlin An and Lei Yang are the co-corresponding authors.

REFERENCES

[1] 2022. AHT10 Integrated temperature and humidity sensor. http://www.aosong.com/en/products-40.html. Accessed: 2022-6-20.
[2] 2022. BFH1K-3EB Full Bridge Strain Gauge. https://www.alibaba.com/product-detail/Taidacent-Customizable-High-Precision-Foil-Resistance_62484048463.html. Accessed: 2022-6-20.
[3] 2022. Ciprian HVA-800-A. https://www.ciprian.com/high-voltage-amplifiers/. Accessed: 2022-1-14.
[4] 2022. Concrete Slab. https://en.wikipedia.org/wiki/Concrete_slab.
[5] 2022. EcoCapsule Project Website. https://ecocapsule.tagsys.org. Accessed: 2022-6-30.
[6] 2022. EPC UHF Gen2 Air Interface Protocol. https://www.gs1.org/standards/rfid/uhf-air-interface-protocol. Accessed: 2022-1-21.
[7] 2022. JLC PCB. https://jlcpcb.com/. Accessed: 2022-1-14.
[8] 2022. LDO Basics. https://www.ti.com/lit/SLYY151A. Accessed: 2022-6-20.
[9] 2022. LP5900SD-1.8. https://www.ti.com/product/LP5900/part-details/LP5900SD-1.8/NOPB. Accessed: 2022-6-20.
[10] 2022. Open-source design of EcoCapsule. https://github.com/Anplus/In-concrete-Backscatter. Accessed: 2022-6-20.
[11] 2022. OWON XDS3000. https://www.owon.com.hk/products_owon_xds3000_series_n-in-1_digital_oscilloscope. Accessed: 2022-1-14.
[12] 2022. Refraction and mode conversion of ultrasonic waves. https://www.olympus-ims.com/en/ndt-tutorials/flaw-detection/wave-front/.
[13] 2022. Rigol DG2052. https://www.rigolna.com/products/waveform-generators/dg2000/. Accessed: 2022-1-14.
[14] 2022. SLA 3D printing materials. https://www.hubs.com/knowledge-base/sla-3d-printing-materials-compared/.
[15] 2022. Solidworks. https://www.solidworks.com/.
[16] 2022. Surfside condominium collapse. https://en.wikipedia.org/wiki/Surfside_condominium_collapse. Accessed: 2022-1-14.
[17] 2022. Ti EnergyTrace Technology. https://www.ti.com/lit/pdf/SLAU157AP. Accessed: 2022-6-20.
[18] 2022. Ti Level Shifter TXB0302. https://www.ti.com/lit/gpn/txb0302. Accessed: 2022-6-20.
[19] 2022. Ti MSP430G2553. https://www.ti.com/product/MSP430G2553. Accessed: 2022-1-14.
[20] 2022. URES. https://help.solidworks.com/2016/english/SolidWorks/cworks/c_Displacement_Reaction_Force_Components.htm.
[21] 2022. YXLON FF35 CT: High Resolution Industrial CT System for Small/Medium-Sized Parts Inspection. https://www.yxlon.com/en/products/x-ray-and-ct-inspection-systems/yxlon-ff35-ct. Accessed: 2022-1-21.
[22] Carlos G Berrocal, Ignasi Fernandez, and Rasmus Rempling. 2021. Crack monitoring in reinforced concrete beams by distributed optical fiber sensors. *Structure and Infrastructure Engineering* 17, 1 (2021), 124–139.

[23] Marc Blumentritt, Kai Melhorn, Johannes Flachsbarth, Michael Kroener, Wolfgang Kowalsky, and Hans-Hermann Johannes. 2008. A novel fabrication method of fiber-optical planar transmission sensors for monitoring pH in concrete structures. *Sensors and Actuators B: Chemical* 131, 2 (2008), 504–508.

[24] Shahram Etemadi Borujeni. 2002. Ultrasonic underwater depth measurement. In *Proceedings of the 2002 Interntional Symposium on Underwater Technology (Cat. No. 02EX556)*. IEEE, 33–36.

[25] Chih-Yuan Chang and San-Shan Hung. 2012. Implementing RFIC and sensor technology to measure temperature and humidity inside concrete structures. *Construction and Building Materials* 26, 1 (2012), 628–637.

[26] Michael T Cunningham, Gary J Saulnier, Robert Chase, Edward M Curt, Kyle R Wilt, Francisco J Maldonado, Stephen Oonk, and Henry A Scarton. 2016. Low-rate ultrasonic communications and power delivery for sensor applications. In *MILCOM 2016-2016 IEEE Military Communications Conference*. IEEE, 91–96.

[27] Jacques Curie and Pierre Curie. 1880. Development by pressure of polar electricity in hemihedral crystals with inclined faces. *Bull. soc. min. de France* 3 (1880), 90.

[28] Jiang Du, Weina Meng, Kamal H Khayat, Yi Bao, Pengwei Guo, Zhenghua Lyu, Adi Abu-obeidah, Hani Nassif, and Hao Wang. 2021. New development of ultra-high-performance concrete (UHPC). *Composites Part B: Engineering* 224 (2021), 109220.

[29] Wen Hui Duan, Quan Wang, and Ser Tong Quek. 2010. Applications of piezoelectric materials in structural health monitoring and repair: Selected research examples. *Materials* 3, 12 (2010), 5169–5194.

[30] Xiaoran Fan, Riley Simmons-Edler, Daewon Lee, Larry Jackel, Richard Howard, and Daniel Lee. 2021. Aurasense: Robot collision avoidance by full surface proximity detection. In *2021 IEEE/RSJ International Conference on Intelligent Robots and Systems (IROS)*. IEEE, 1763–1770.

[31] Reza Ghaffarivardavagh, Sayed Saad Afzal, Osvy Rodriguez, and Fadel Adib. 2020. Ultra-wideband underwater backscatter via piezoelectric metamaterials. In *Proc. of ACM SIGCOMM*. 722–734.

[32] Zachary C Grasley, David A Lange, and DD Matthew. 2006. Internal relative humidity and drying stress gradients in concrete. *Materials and Structures* 39, 9 (2006), 901–909.

[33] Baoguo Han, Siqi Ding, and Xun Yu. 2015. Intrinsic self-sensing concrete and structures: A review. *Measurement* 59 (2015), 110–128.

[34] Xin Huang, Jafar Saniie, Sasan Bakhtiari, and Alexander Heifetz. 2018. Applying EMAT for ultrasonic communication through steel plates and pipes. In *2018 IEEE International Conference on Electro/Information Technology (EIT)*. IEEE, 0379–0383.

[35] Vikram Iyer, Vamsi Talla, Bryce Kellogg, Shyamnath Gollakota, and Joshua Smith. 2016. Inter-technology backscatter: Towards internet connectivity for implanted devices. In *Proc. of ACM SIGCOMM*. 356–369.

[36] Junsu Jang and Fadel Adib. 2019. Underwater backscatter networking. In *Proc. of ACM SIGCOMM*. 187–199.

[37] Sergej Johann, Christoph Strangfeld, Maximilian Müller, Björn Mieller, and Matthias Bartholmai. 2017. RFID sensor systems embedded in concrete–requirements for long–term operation. *Materials Today: Proceedings* 4, 5 (2017), 5827–5832.

[38] Soonwon Ka, Tae Hyun Kim, Jae Yeol Ha, Sun Hong Lim, Su Cheol Shin, Jun Won Choi, Chulyoung Kwak, and Sunghyun Choi. 2016. Near-ultrasound communication for tv's 2nd screen services. In *Proc. of ACM MobiCom*. 42–54.

[39] R Kishore. 1968. Acoustic attenuation in solids. *Physical Review* 173, 3 (1968), 856.

[40] Jodie Y Lee, PK Goh, and William H Lam. 2005. New level-of-service standard for signalized crosswalks with bi-directional pedestrian flows. *Journal of transportation engineering* 131, 12 (2005), 957–960.

[41] Young Hak Lee and Taekeun Oh. 2016. The measurement of P-, S-, and R-wave velocities to evaluate the condition of reinforced and prestressed concrete slabs. *Advances in Materials Science and Engineering* 2016 (2016).

[42] Qiongzheng Lin, Zhenlin An, and Lei Yang. 2019. Rebooting ultrasonic positioning systems for ultrasound-incapable smart devices. In *Proc. of ACM MobiCom*. 1–16.

[43] Vincent Liu, Aaron Parks, Vamsi Talla, Shyamnath Gollakota, David Wetherall, and Joshua R Smith. 2013. Ambient backscatter: Wireless communication out of thin air. *Proc. ACM SIGCOMM* 43, 4 (2013), 39–50.

[44] Jerome P Lynch and Kenneth J Loh. 2006. A summary review of wireless sensors and sensor networks for structural health monitoring. *Shock and Vibration Digest* 38, 2 (2006), 91–130.

[45] Yunfei Ma, Nicholas Selby, and Fadel Adib. 2017. Drone relays for battery-free networks. In *Proc. of ACM SIGCOMM*. 335–347.

[46] Sidney Mindess. 2019. *Developments in the Formulation and Reinforcement of Concrete*. Woodhead Publishing.

[47] Peter Oppermann and Christian Renner. 2019. Low-Power Ultrasonic Wake-Up and Communication through Structural Elements. In *Proceedings of the 7th International Workshop on Energy Harvesting & Energy-Neutral Sensing Systems*. 42–48.

[48] Yao Peng, Longfei Shangguan, Yue Hu, Yujie Qian, Xianshang Lin, Xiaojiang Chen, Dingyi Fang, and Kyle Jamieson. 2018. PLoRa: A passive long-range data network from ambient LoRa transmissions. In *Proc. of ACM SIGCOMM*. 147–160.

[49] Nirupam Roy, Mahanth Gowda, and Romit Roy Choudhury. 2015. Ripple: Communicating through physical vibration. In *Proc. of USENIX NSDI*. 265–278.

[50] Gary J Saulnier, Henry A Scarton, Andrew J Gavens, DA Shoudy, TL Murphy, M Wetzel, S Bard, S Roa-Prada, and P Das. 2006. P1g-4 through-wall communication of low-rate digital data using ultrasound. In *2006 IEEE Ultrasonics Symposium*. IEEE, 1385–1389.

[51] Dongjin Seo, Ryan M Neely, Konlin Shen, Utkarsh Singhal, Elad Alon, Jan M Rabaey, Jose M Carmena, and Michel M Maharbiz. 2016. Wireless recording in the peripheral nervous system with ultrasonic neural dust. *Neuron* 91, 3 (2016), 529–539.

[52] Sam Siu, Qing Ji, Wenhao Wu, Gangbing Song, and Zhi Ding. 2014. Stress wave communication in concrete: I. Characterization of a smart aggregate based concrete channel. *Smart materials and structures* 23, 12 (2014), 125030.

[53] Christoph Strangfeld, Sergej Johann, and Matthias Bartholmai. 2019. Smart RFID sensors embedded in building structures for early damage detection and long-term monitoring. *Sensors* 19, 24 (2019), 5514.

[54] Karthick Subbiah, Saraswathy Velu, Seung-Jun Kwon, Han-Seung Lee, Natarajan Rethinam, and Dong-Jin Park. 2018. A novel in-situ corrosion monitoring electrode for reinforced concrete structures. *Electrochimica Acta* 259 (2018), 1129–1144.

[55] Ye Sun, Chen-Yuan Chung, Xiong Bill Yu, Zhen Liu, Yan Liu, and Junliang Tao. 2013. Advanced Ultrasonic Technology for Air Void Distribution in Concrete. *Materials Evaluation* 71, 3 (2013).

[56] Shima Taheri. 2019. A review on five key sensors for monitoring of concrete structures. *Construction and Building Materials* 204 (2019), 492–509.

[57] Jin-Guang Teng, Yu Xiang, Tao Yu, and Zhi Fang. 2019. Development and mechanical behaviour of ultra-high-performance seawater sea-sand concrete. *Advances in Structural Engineering* 22, 14 (2019), 3100–3120.

[58] Boyang Wang, Jafar Saniie, Sasan Bakhtiari, and Alexander Heifetz. 2019. Ultrasonic communication systems for data transmission. In *2019 IEEE International Conference on Electro Information Technology (EIT)*. IEEE, 1–4.

[59] Qi Xia, Wang-lin Wu, Fu-nian Li, Yong Xia, Xiao-li Ding, William HK Lam, Weng-hong Chung, and You-lin Xu. 2021. System design and demonstration of performance monitoring of a butterfly-shaped arch footbridge. *Structural Control and Health Monitoring* 28, 7 (2021), e2738.

[60] Xieyang Xu, Yang Shen, Junrui Yang, Chenren Xu, Guobin Shen, Guojun Chen, and Yunzhe Ni. 2017. Passivevlc: Enabling practical visible light backscatter communication for battery-free iot applications. In *Proc. of ACM MobiCom*. 180–192.

[61] Nazli Yesiller, Tuncer B Edil, and Craig H Benson. 1997. Ultrasonic method for evaluation of annular seals for wells and instrument holes. *Geotechnical Testing Journal* 20, 1 (1997), 17.

[62] Zhijia You and Lingjun Feng. 2020. Integration of industry 4.0 related technologies in construction industry: a framework of cyber-physical system. *IEEE Access* 8 (2020), 122908–122922.

[63] B Zhang, Jin Guang Teng, and Tao Yu. 2017. Compressive behavior of double-skin tubular columns with high-strength concrete and a filament-wound FRP tube. *Journal of Composites for Construction* 21, 5 (2017), 04017029.

[64] Renjie Zhao, Purui Wang, Yunfei Ma, Pengyu Zhang, Hongqiang Harry Liu, Xianshang Lin, Xinyu Zhang, Chenren Xu, and Ming Zhang. 2020. Nfc+ breaking nfc networking limits through resonance engineering. In *Proc. of ACM SIGCOMM*. 694–707.

[65] Tianyue Zheng, Zhe Chen, Jun Luo, Lin Ke, Chaoyang Zhao, and Yaowen Yang. 2021. SiWa: see into walls via deep UWB radar. In *Proc. of ACM MobiCom*. 323–336.

[66] Zhupeng Zheng, Xiaoning Sun, and Ying Lei. 2009. Monitoring corrosion of reinforcement in concrete structures via fiber Bragg grating sensors. *Frontiers of Mechanical Engineering in China* 4, 3 (2009), 316–319.

[67] Lu Zhou, Si-Xin Chen, Yi-Qing Ni, and Alex Wai-Hing Choy. 2021. EMI-GCN: a hybrid model for real-time monitoring of multiple bolt looseness using electromechanical impedance and graph convolutional networks. *Smart Materials and Structures* 30, 3 (2021), 035032.

APPENDIX

Appendices are supporting material that has not been peer-reviewed. Appendices include supporting materials for the system design, implementation, and evaluation results.

A BACKGROUND OF BODY WAVES

Fig. 23 visually illustrates the P-wave and S-wave. In short, P-waves travel faster, move in a push-pull pattern, travel through solids, liquids, and gases, easier to attenuate, while S-waves travel slower,

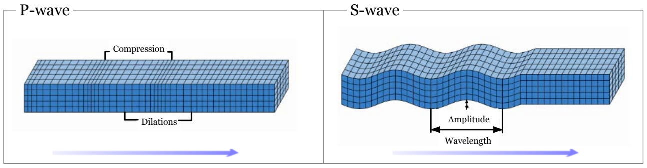

Fig. 23: Illustration of two modes of body waves

move in an up-and-down pattern, travel only through solids, and spread farther. The two modes of a body wave can be simply regarded as two copies of the input wave, traveling with two different physical forms and two speeds.

Here, we show the body wave equations. Suppose **u** is the displacement, ρ is the density of the travel media, λ and μ are the Lamé parameters. Then the body wave momentum equaiton when travelling in homogeneous media can be fomulated as:

$$\rho \ddot{\mathbf{u}} = (\lambda + 2\mu)\nabla\nabla \cdot \mathbf{u} - \mu\nabla \times \nabla \times \mathbf{u}. \tag{6}$$

We can separate this equation into solutions for P-waves and S-waves by taking the divergence and curl, respectively, and using several vector identities. The resulting P-wave equation is

$$\nabla^2(\nabla \cdot \mathbf{u}) - \frac{1}{\alpha^2}\frac{\partial^2(\nabla \cdot \mathbf{u})}{\partial t^2} = 0 \tag{7}$$

where the P-wave velocity, α, is given by

$$\alpha = \sqrt{\frac{\lambda + 2\mu}{\rho}} \tag{8}$$

The corresponding S-wave equation is

$$\nabla^2(\nabla \times \mathbf{u}) - \frac{1}{\beta^2}\frac{\partial^2(\nabla \times \mathbf{u})}{\partial t^2} = 0 \tag{9}$$

where the S-wave velocity, β, is given by

$$\beta = \sqrt{\frac{\mu}{\rho}} \tag{10}$$

B PROPERTIES OF TESTED CONCRETE

In our evaluation, we tested three kinds of concrete. Their mix proportions and properties are listed in Table. 1. To the best of the authors' knowledge, the UHPFRC records the strongest concrete produced with standard mixing and curing techniques.

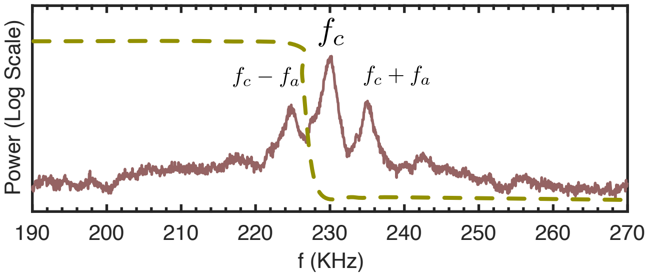

Fig. 24: Self-interference elimination

Table 1: Mix proportions and properties of concretes used in our experiments. In the table, HRWR is the high range water reducers, f_{co} is the compressive strength, E_c is the concrete elastic modulus, ν is the Poisson's ratio, and ϵ_{co} is the corresponding strain.

#	Concretes	NC	UHPC	UHPSSC
Mix proportions	Cement	300	830	807
	Silica Fume	0	207	202
	Fly Ash	200	0	0
	Quartz Power	0	207	202
	Sand	796	913	888
	Granite	829	0	0
	Steel Fiber	0	0	471
	Water	175	164	158
	HRWR	9	27	29
Properties	f_{co}(MPa)	54.1	195.3	215.0
	E_c(GPa)	27.8	52.5	52.7
	ν	0.18	0.21	0.21
	ϵ_{co}(%)	0.263	0.447	0.447

C SELF-INTERFERENCE IN UPLINK

Fig. 24 shows the spectrum of the received signals, in which we can precisely observe three peaks. One peak is from the CBW. No signal at non-resonant frequency is detected during the backscatter period in the uplink. The other two peaks are from the two sides AM of the backscatter signals. There is a guard band to separate the two signals.

Table 2: Level of structural health based on pedestrian area occupancy. (m^2/ped). This table shows the relationship between average area on the bridge occupied by each pedestrian and the degree of health of the bridge in different regions or countries.

Health	United States	Hong Kong	Bangkok	Manila
A	>3.85	>3.25	>2.38	>3.25
B	3.85-2.3	3.85-2.16	2.38-1.60	3.25-2.05
C	2.30-1.39	2.16-1.40	1.60-0.98	2.05-1.65
D	1.39-0.93	1.40-0.80	0.98-0.65	1.65-1.25
E	0.93-0.46	0.80-0.52	0.65-0.37	1.25-0.56
F	<0.46	<0.52	<0.37	<0.56

D HEALTH MONITORING OF A REAL LIFE FOOTBRIDGE

The level of health on different sections of the footbridge is graded based on the resultant pedestrian area occupancy (PAO) and updated once every minute. The full definition of PAO can refer to [40]. In short, six health levels of service (A to F) are designated for walking facilities. The maximum average PAO cannot be less than 1 m^2/ped. Otherwise, the bridge might be seriously damaged or even collapse. Fig. 25 shows the detailed layout of the sensors installed on the bridge. It contains 88 conventional external sensors. The monitoring items are grouped into three categories: environmental parameters (air temperature, air pressure, humidity, rain, and solar radiation), loads (winds and structural temperature), and bridge responses (stress/strain, displacement, and acceleration). Particularly, we show the response data acquired in July 2021 in Fig. 29 to Fig. 36.

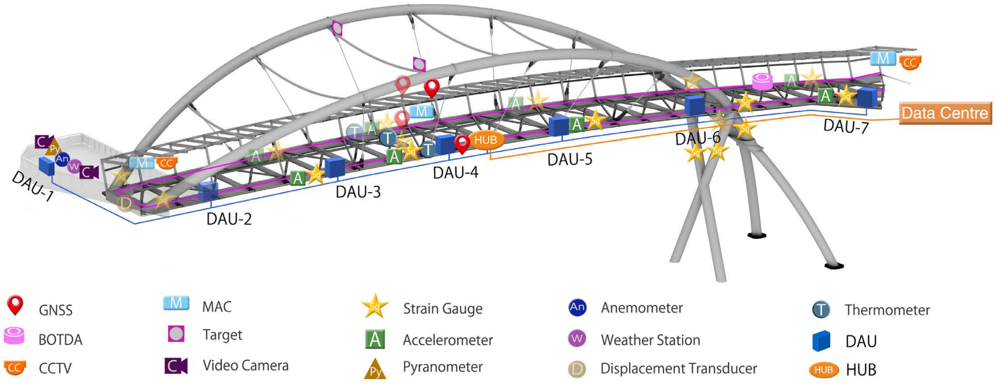

Fig. 25: Layout of sensors deployed on the bridge [59]

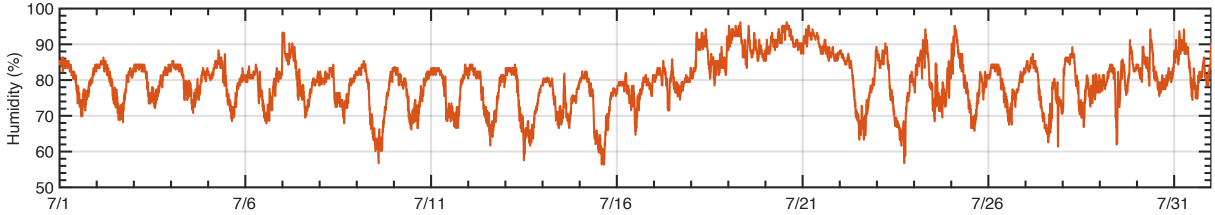

Fig. 26: Humidity Sensor

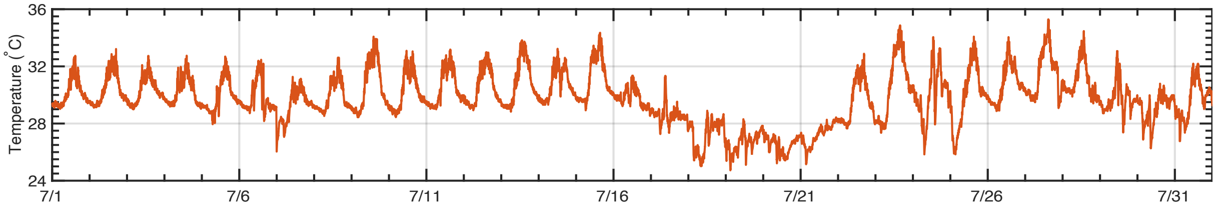

Fig. 27: Temperature Sensor

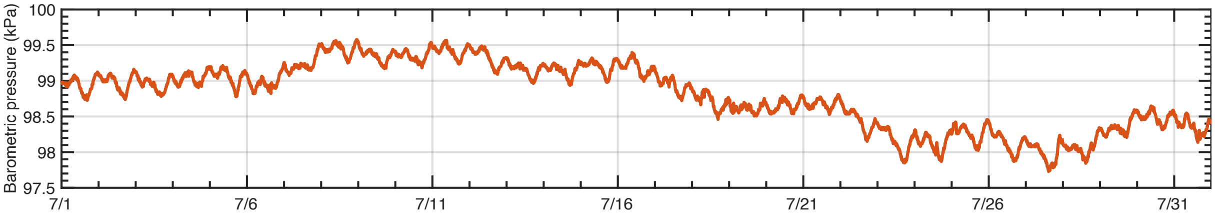

Fig. 28: Barometric Pressure Sensor

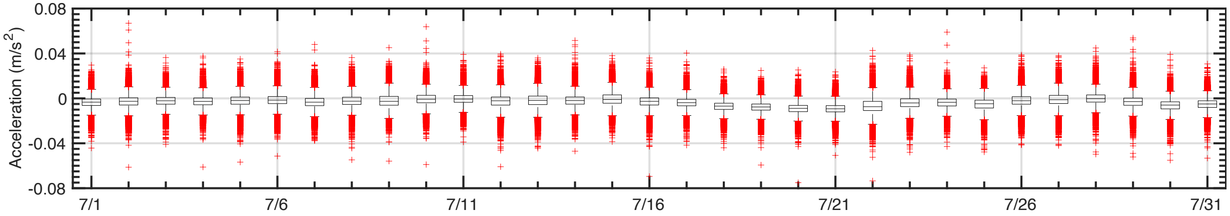

Fig. 29: Acceleration from Sensor #1

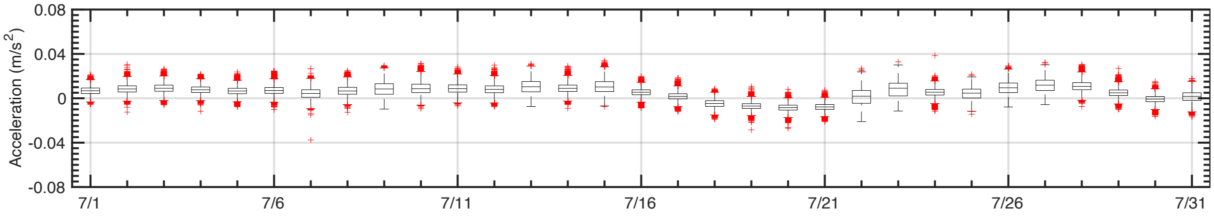

Fig. 30: Acceleration from Sensor #2

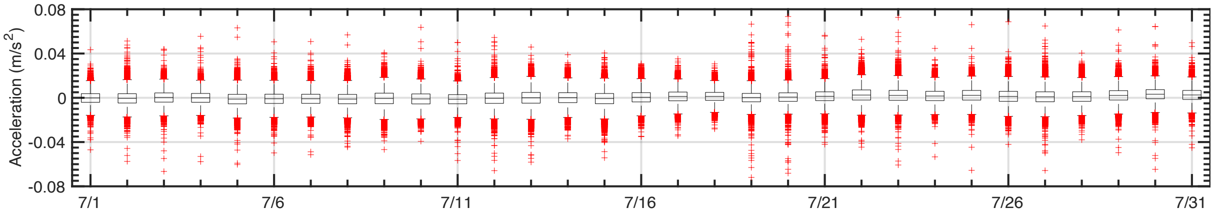

Fig. 31: Acceleration from Sensor #3

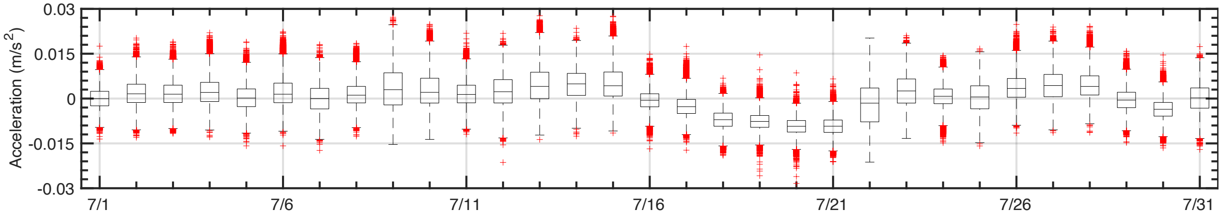

Fig. 32: Accelerometer from Sensor #4

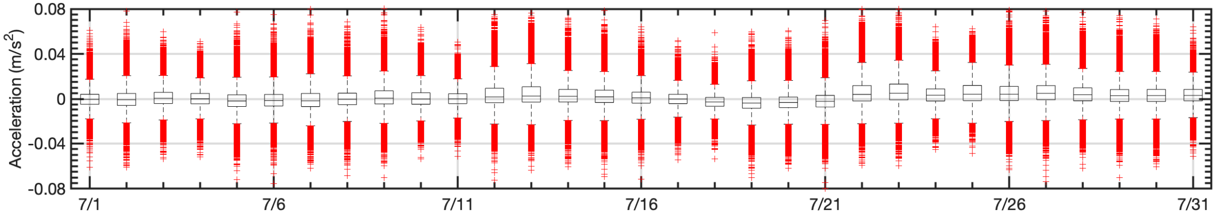

Fig. 33: Acceleration from Sensor #5

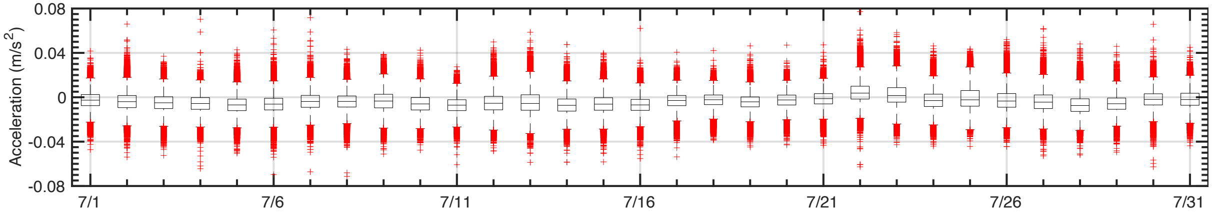

Fig. 34: Acceleration from Sensor #6

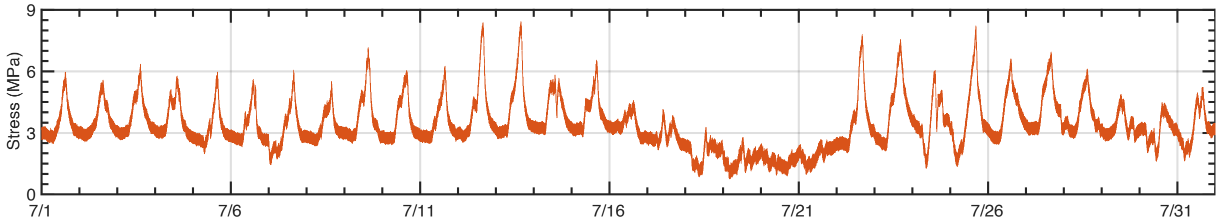

Fig. 35: Stress measurements from Sensor #1

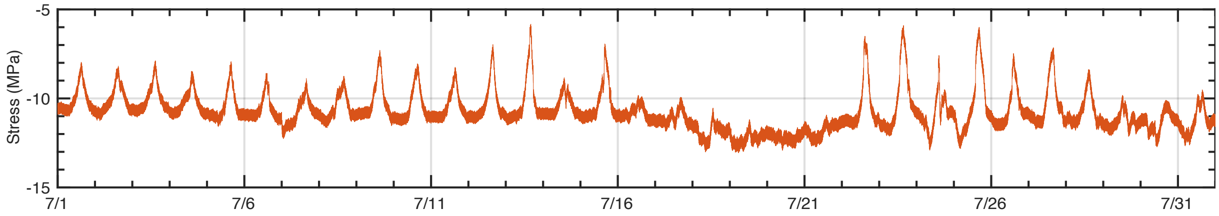

Fig. 36: Stress measurements from Sensor #2